On the Spectral Efficiency of Orbital Angular Momentum With Mode Offset

Ahmed Almradi, Muhammad Ali Babar Abbasi, *Member, IEEE*, Michail Matthaiou, *Senior Member, IEEE*, and Vincent F. Fusco, *Fellow, IEEE*

***Abstract*—Thanks to its low transceiver complexity, mode division multiplexing (MDM) using orbital angular momentum (OAM) has been recently investigated as a new physical layer wireless transmission technique. This is due to the fact that different OAM modes are spatially orthogonal to each other, thus, perfectly suitable for spatial multiplexing and/or diversity. The orthogonality amongst different OAM modes is achieved in the absence of any mode offset between the transceivers' phase-shifting feeding networks. However, the inherent presence of OAM mode offset destroys the orthogonality between different modes, which gives rise to inter-mode interference (IMI). Therefore, in this paper, in order to theoretically analyze the negative impact of OAM mode offset of MDM-OAM systems on the spectral efficiency of line-of-sight free-space wireless communication systems, an explicit signal-to-interference-plus-noise ratio expression for each OAM mode is derived, through which the spectral efficiency degradation is evaluated. Furthermore, in order to support our theoretical analysis, a 9×9 MDM-OAM practical communication experiment for different OAM mode settings is carried out at a microwave frequency of 5.8 GHz. In addition, by leveraging the fact that all circulant matrices always have the same eigendirections, regardless of the entries of the matrix, a low-complexity optimal OAM mode selection scheme is proposed which significantly improves the spectral efficiency of the system. Finally, in order to completely null-out the impact of OAM mode offset, a baseband zero-forcing stage is embedded at the receiver.**

***Index Terms*—Mode division multiplexing, multiple-input-multiple-output systems, orbital angular momentum, spatial multiplexing, uniform circular antenna array, zero-forcing.**

I. Introduction

IN ORDER to significantly increase the spectral efficiency over the same time–frequency resources, spatial division multiplexing (SDM) based multiple-input multiple-output (MIMO) systems have been traditionally considered as the most promising solution. However, such systems not only require a dedicated radio-frequency (RF) chain for each antenna element, which results in high cost and power consumption (a key bottleneck especially for millimeter wave (mmWave) massive MIMO), but they also suffer from severe inter-channel interference (ICI), which requires a complicated transceiver digital baseband signal processing (i.e., a dedicated transmit precoding and receive combining matrices), see e.g., [1]–[4]. To alleviate these issues, orbital angular momentum (OAM) has been recently proposed, by which multiple information streams can be simultaneously transmitted over the same time–frequency resources in a mode division multiplexing (MDM) manner [5]–[9]. For a uniform circular antenna array (UCA), fed with the same input signal and a successive phase delay from element to element of $2\pi l/N$, where N is the number of antenna elements in the UCA and l is the OAM mode number, a vortex beam (OAM signal with helical wavefront) can be generated in a specified direction perpendicular to the UCA plane. It was proved in [7] and [10] that OAM based MDM does not offer any additional spectral efficiency gains when compared against the traditional fully digital MIMO systems. However, due to its low cost and power consumption, as well as low transceiver complexity, OAM-MDM systems are considered as an appealing physical layer candidate for short-range free-space wireless communications in the mmWave and terahertz spectrum [5], [11]. Moreover, in order to further improve the spectral efficiency of the system, a combination between OAM-MDM multiplexing and MIMO-SDM has been investigated in [11]. Furthermore, the combination between OAM and orthogonal frequency division multiplexing (OFDM) has been proposed in [12] and [13] to achieve high spectral efficiency in sparse multipath fading channels.

An experimental MDM-OAM study was pursued in [10]. It was shown that MDM-OAM is a promising low-complexity candidate for free-space short distance wireless communications. OAM mode orthogonality has been investigated in [9]. The combination of OAM with index modulation has been considered in [6]. The impact of transmit and receive UCAs' misalignment on the performance of OAM systems has been studied in [8]. More recently, the authors in [14] proposed an optimal UCA design by selecting the optimal OAM modes and radius of the receive UCA which maximizes the system capacity. Note that in order to generate an OAM signal, a phase-shifting network (PSN) is required with the transmit UCA to excite each data stream with a specified OAM mode. This can be efficiently

---

Manuscript received September 25, 2020; revised March 5, 2021 and August 1, 2021; accepted September 6, 2021. Date of publication September 21, 2021; date of current version November 18, 2021. The work of Ahmed Almradi was supported in part by the U.K. Engineering and Physical Sciences Research Council (EPSRC) under Grant EP/P000673/1 and in part by U.K. Research and Innovation Future Leaders Fellowships under Grant MR/T019980/1. The work of Michail Matthaiou was supported in part by a research grant from the Department for the Economy Northern Ireland under the US-Ireland Research and Development Partnership Programme and in part by European Research Council (ERC) under the European Union's Horizon 2020 research, and innovation programme under Grant Agreement 101001331. The review of this article was coordinated by Prof. Ha H. Nguyen. *(Corresponding author: Ahmed Almradi.)*

Ahmed Almradi is with the BT Labs, Ipswich IP5 3RE, U.K. (e-mail: ahmed.almradi@bt.com).

Muhammad Ali Babar Abbasi, Michail Matthaiou, and Vincent F. Fusco are with the Institute of Electronics, Communications, and Information Technology (ECIT), Queen's University, Belfast BT3 9DT, U.K. (e-mail: m.abbasi@qub.ac.uk; m.matthaiou@qub.ac.uk; v.fusco@ecit.qub.ac.uk).

Digital Object Identifier 10.1109/TVT.2021.3113983

implemented by a Butler matrix, i.e., a discrete Fourier transform (DFT) matrix. Similarly, in order to recover the transmitted OAM signal at the receiver, the receive UCA is connected with a PSN which is characterized by an inverse discrete Fourier transform (IDFT) matrix. When the UCAs at the transmitter and receiver end are aligned, the attractive advantage of MDM-OAM is that the free-space wireless propagation channel matrix becomes a circulant matrix, i.e., each row of the channel matrix is a right circular (cyclic) shift of the first row. Circulant matrices have the appealing property that they always have the same orthonormal eigenvectors (eigendirections), hence, can be efficiently and perfectly diagonalized by a fixed unitary DFT and IDFT matrix [15]. As such, the OAM channel eigenmode decomposition can simply be designed by fixed analog transmit precoding and receive combining matrices based on DFT and IDFT matrices with fixed phase shifters, respectively. It is to be emphasized that traditional fully digital and hybrid analog and digital MIMO systems require accurate channel state information at the transmitter (CSIT) in order to diagonalize the channel using singular value decomposition (SVD),[1] whereas no CSIT is required for MDM-OAM [7], [10].

Conventional MDM-OAM systems, which activate all available OAM modes, require a dedicated RF chain for each antenna element (see e.g., [8], [16]), thus, resulting in high cost and power consumption. To alleviate these issues, given that systems operating in the mmWave and terahertz frequencies require high beamforming gain in order to compensate for their severe pathloss, a hybrid analog and digital precoding system, where a much smaller number of RF chains are connected to a massive number of antennas via a set of low power and cost analog phase shifters, could be leveraged instead [3], [4]. In order for the mode orthogonality to hold at the receiver, the receive PSN (IDFT matrix) must be aligned with the transmit PSN (DFT matrix). It is well known that the OAM waveform can be generated via phase controlled excitation of antennas and this can be achieved by following the general MIMO concept, where each antenna element is separately excited [7]. However, separate antenna excitation is sometimes not practical due to hardware limitations. In this case, antennas can be alternatively excited via PSNs, which are responsible for generating excitation conditions that mimic the ideal OAM mode generation conditions [17]–[20]. However, PSNs are not ideal since they have inherent imperfections (e.g. quantization errors, loss of imbalance, mismatch loss, etc.). Therefore, perfect OAM mode excitation is challenging in practice and an OAM mode offset is inevitable. Hence, an OAM mode offset resulting from the mismatch (synchronization error) between the excited OAM modes at the transmit and receive PSNs exists in practice. Under these circumstances, we observe leakage of information transmitted by one OAM mode into the other mode(s). In other words, the modes offset from the ideal conditions due the impairments in the hardware, which compromises the theoretically idealized, simultaneous data transmission via orthogonal modes. Understanding and analyzing the OAM mode offset is important in order to quantify the magnitude of this phenomenon on the spectral efficiency of the OAM systems. From the above discussion, we can infer that MDM-OAM is intrinsically susceptible to OAM mode offset, which destroys the orthogonality between different OAM modes, bringing about inter-mode interference (IMI) which deteriorates the spectral efficiency of the system. Consequently, given that activating all OAM modes is not always optimal, since some OAM eigenmodes are extremely small and result in very low received OAM signal power, and in order to reduce the cost and power consumption of OAM systems, a DFT based hybrid precoding OAM system is envisioned herein where the $N \times N$ analog DFT matrix is connected to only M RF chains, where $M \leq N$, via a low cost and power switching network for OAM mode selection. Hence, over the same time–frequency resources, out of the N available OAM modes, a maximum of M OAM modes (symbols) can be activated (transmitted) through the M RF chains.

To this end and in the presence of OAM mode offset, we first design the transmit analog DFT precoder based on an arbitrary OAM mode selection scheme, i.e., by arbitrarily activating the first M OAM modes of the transmit DFT matrix. It is shown that an OAM mode offset can severely degrade the spectral efficiency of the system, thus, an OAM mode offset estimation and compensation technique is required at the receiver.

The main contributions of this paper can be summarized as follows:

1) In the presence of OAM mode offset, a new explicit signal-to-interference-plus-noise ratio (SINR) expression is derived for each OAM mode, through which the spectral efficiency degradation is investigated. The analytically friendlier case of constant OAM mode offset is considered first, which is then extended to the general case of random OAM mode offset.
2) In order to achieve the optimal maximum spectral efficiency, and motivated by the eigenvalue decomposition of the OAM channel, we propose a low-complexity optimal OAM mode selection scheme, where the OAM modes corresponding to the dominant eigendirections of the channel are activated.
3) We experimentally demonstrate a 9×9 MDM-OAM communication link using OAM mode multiplexing at a microwave frequency of 5.8 GHz. More specifically, a 9 element patch antenna circular array capable of generating spatially orthogonal OAM modes is developed. In order to predict the measurement OAM mode offset, we utilize the correlation matrix distance measure between the theory and measurement OAM mode correlations.
4) In order to fully cancel out the impact of OAM mode offset, a low complexity digital baseband zero-forcing (ZF) receiver is proposed.

A. Paper Organization

Section II introduces the system and channel model. In Section III, the overall SINR is presented, whereas Section IV considers the OAM mode selection scheme. Section V presents the ZF receiver, and Section VI introduces the experimental

---

[1] Traditionally, the optimal performance is achieved by utilizing a transmit precoder that is aligned with the channel right singular vectors, and a receive combiner that is aligned with the channel left singular vectors. Therefore, SVD based OAM systems require a phase-shifting network with variable phase entries. Consequently, high precision variable phase shifters are required in order to design the transmit and receive analog precoders. Note that non-circulant channel matrices have different eigenvectors.

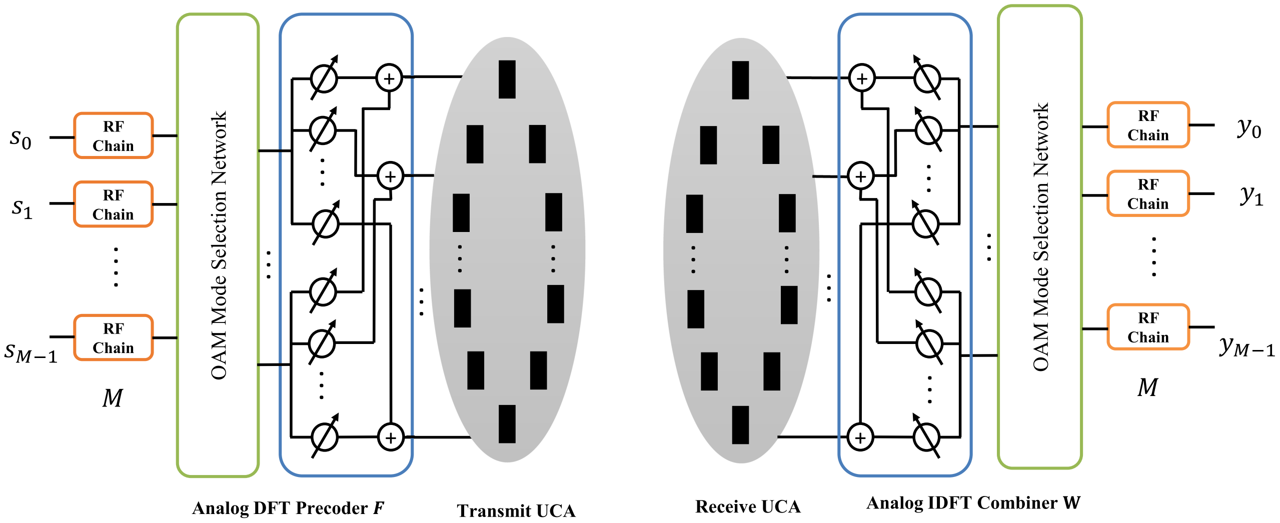

Fig. 1. The OAM system model.

results. Section VII presents the numerical results and comparison between theory and measurements, while Section VIII concludes the paper.

B. Notations

Bold lower (upper) case letters denote vectors (matrices). The notations $\boldsymbol{X}^T$, $\boldsymbol{X}^\dagger$, $\boldsymbol{X}^{-1}$, $\boldsymbol{X}^+$, and $\mathrm{Tr}(\boldsymbol{X})$ denote the transpose, conjugate transpose, inverse, pseudo-inverse, and trace of a matrix $\boldsymbol{X}$, respectively, while $\boldsymbol{I}_N$ is the $N \times N$ identity matrix. Also, $[\boldsymbol{X}]_{m,n}$ and $\measuredangle[\boldsymbol{X}]_{m,n}$ denote the $(m,\, n)^{\text{th}}$ element of the matrix $\boldsymbol{X}$ and its phase, $\|\boldsymbol{X}\|_F$ denotes the Frobenius norm of the matrix $\boldsymbol{X}$; $\|\cdot\|$ and $|\cdot|$ denote the Euclidean ℓ_2 norm and absolute value operators, respectively; $\mathbb{E}[\cdot]$ denotes the expectation operator, whereas $\mathrm{diag}(x_1,\, x_2,\, \ldots,\, x_N)$ denotes a diagonal matrix with diagonal elements $\{x_1,\, x_2,\, \ldots,\, x_N\}$.

II. SYSTEM AND CHANNEL MODEL

As shown in Fig. 1, we consider two aligned UCAs equipped with N antenna elements, connected to a network of fixed phase shifters and an OAM mode selection mechanism. To transmit an OAM signal with mode number l, the OAM mode selection network activates the column corresponding to the l^{th} mode from the DFT network matrix, hence, the same input signal s_l needs to be applied to all the transmit UCA elements with a successive phase shift excitation applied at each element. Thus, the l^{th} mode signal applied to the n^{th} transmit antenna can be written as

$$x_{l,n} = \frac{1}{\sqrt{N}}\sqrt{p_l}s_l e^{-j\frac{2\pi nl}{N}}, n = 0,\, \ldots,\, N-1, \qquad (1)$$

where p_l is the power allocated to the l^{th} mode signal s_l, and $\varphi_n = \frac{2\pi n}{N}$ is the azimuth angle corresponding to the n^{th} transmit antenna. In the MDM-OAM scheme, each transmit antenna is fed by a superposition of the OAM signals along all excited modes. Thus, the composite transmitted signal applied to the n^{th} transmit antenna is given as

$$x_n = \sum_{l=0}^{M-1} x_{l,n} = \frac{1}{\sqrt{N}}\sum_{l=0}^{M-1}\sqrt{p_l}s_l e^{-j\frac{2\pi nl}{N}}, n = 0,\, \ldots,\, N-1, \qquad (2)$$

where M denotes the number of excited OAM modes, upper bounded by the number of RF chains $M \leq N$.

The PSN excites the l^{th} mode signal to the n^{th} transmit antenna according to $\frac{1}{\sqrt{N}}e^{-j\frac{2\pi nl}{N}}$. Thus, OAM mode multiplexing (demultiplexing) can be realized by a DFT (IDFT) matrix. Therefore, the composite MDM-OAM transmitted signal and the received signal (before IDFT combining) are respectively given as

$$\boldsymbol{x} = \boldsymbol{F}\boldsymbol{P}\boldsymbol{s} = \sum_{l=0}^{M-1}\sqrt{p_l}s_l\boldsymbol{f}_l, \qquad (3)$$

$$\boldsymbol{r} = \boldsymbol{H}\boldsymbol{F}\boldsymbol{P}\boldsymbol{s} + \boldsymbol{n}, \qquad (4)$$

where $\boldsymbol{s} \in \mathbb{C}^{M\times 1} = [s_0 \quad s_2 \quad \ldots \quad s_{M-1}]^T$ is the transmitted data symbol vector along the activated OAM orthogonal modes, with entries that are independent and identically distributed (i. i. d.) Gaussian random variables with zero mean and unit variance, while $\boldsymbol{H} \in \mathbb{C}^{N\times N}$ is the free-space line-of-sight (LOS) wireless propagation channel matrix between the transmit and receive UCAs. The transmit PSN constitutes a fixed unitary DFT matrix $\boldsymbol{U} \in \mathbb{C}^{N\times N}$, through which only M modes (columns) are activated via the OAM mode selection network, resulting in a semi-unitary DFT matrix of[2] $\boldsymbol{F} \in \mathbb{C}^{N\times M} = [\boldsymbol{f}_0 \quad \boldsymbol{f}_1 \quad \ldots \quad \boldsymbol{f}_{M-1}]$, with $\boldsymbol{f}_l = \frac{1}{\sqrt{N}}[1 \quad e^{-j\frac{2\pi l}{N}} \quad \ldots \quad e^{-j\frac{2\pi(N-1)l}{N}}]^T$, $\boldsymbol{n}$ is the additive white Gaussian noise (AWGN) distributed according to $\boldsymbol{n} \sim \mathcal{CN}(0,\, \sigma^2\boldsymbol{I}_N)$, and $\boldsymbol{P} = \mathrm{diag}(\sqrt{p_0},\, \sqrt{p_1},\, \ldots,\, \sqrt{p_{M-1}})$ is a diagonal power allocation matrix. Similarly, the receive PSN constitutes a fixed unitary IDFT matrix $\boldsymbol{V} \in \mathbb{C}^{N\times N}$, by which only

---

[2] In this section, we assume a fixed OAM mode selection network, where only the first M modes are activated blindly, i.e., $l \in \{0,\, 1,\, \ldots,\, M-1\}$. An optimal OAM mode selection network is introduced in Section IV.

the same OAM modes activated in $\boldsymbol{F}$ are utilized by the OAM mode selection network, resulting in a semi-unitary IDFT matrix $\boldsymbol{W}^{\dagger} \in \mathbb{C}^{M\times N}$, where $\boldsymbol{W} = [\boldsymbol{w}_0 \ \ \boldsymbol{w}_1 \ \ \dots \ \ \boldsymbol{w}_{M-1}]$, with $\boldsymbol{w}_l = \frac{1}{\sqrt{N}}[1 \ \ e^{-j\frac{2\pi(l+\epsilon)}{N}} \ \ \dots \ \ e^{-j\frac{2\pi(N-1)(l+\epsilon)}{N}}]^T$, and ϵ denotes the fixed OAM mode offset, which can potentially result from synchronization error.

Given that the transmit OAM signals are constrained to their maximum power P, the total transmit signal power is normalized such that

$$\begin{aligned}\mathbb{E}\left[\left\|\sum_{l=0}^{M-1}\sqrt{p_l}\boldsymbol{f}_l s_l\right\|^2\right] &= \sum_{l=0}^{M-1}\sum_{k=0}^{M-1}\sqrt{p_l}\sqrt{p_k}\boldsymbol{f}_l^{\dagger}\boldsymbol{f}_k\mathbb{E}\left[s_l^{\dagger}s_k\right]\\ &= \sum_{l=0}^{M-1}p_l\left\|\boldsymbol{f}_l\right\|^2 = P. \end{aligned} \tag{5}$$

Given that the l^{th} mode analog precoder's ℓ_2 norm satisfies $\|\boldsymbol{f}_l\| = 1$, the power constraint in (5) reduces to $\sum_{l=0}^{M-1} p_l = P$.

The free-space wireless propagation channel between the n^{th} transmit UCA antenna and the m^{th} receive UCA antenna is defined as

$$h_{mn} = [\boldsymbol{H}]_{m,n} = \beta\frac{\lambda}{4\pi d_{mn}}e^{-j\frac{2\pi d_{mn}}{\lambda}}, \tag{6}$$

where λ is the wavelength, β is a constant denoting the antenna gain, d_{mn} is the distance between the n^{th} transmit antenna and the m^{th} receive antenna, which in the case of perfect transmitter and receiver UCAs alignment, is given by

$$d_{mn} = \sqrt{D^2 + R_T^2 + R_R^2 - 2R_T R_R\cos\left(\frac{2\pi}{N}(n-m)\right)}, \tag{7}$$

where D denotes the distance between the transmitter and receiver circular array centers, whilst R_T and R_R are, respectively, the radii of the transmit and receive UCAs.

Due to the symmetry between the transmit UCA and receive UCA antennas, the channel matrix $\boldsymbol{H}$ is a circulant matrix. The eigenvectors of all circulant matrices are always the same regardless of the entries of the matrix. Therefore, circulant matrices can be efficiently diagonalized by unitary fixed analog DFT and IDFT matrices [15].

A. Circulant Channel Matrices

Circulant matrices are a special case of Toeplitz matrices, and are simply defined by their first row, given as $\boldsymbol{h} = [h_0 \ \ h_1 \ \ \dots \ \ h_{N-1}]^T$, where each row is a cyclic shift to the right by one position of the previous one. Therefore, the entries of $\boldsymbol{h}$ are called the generating elements of the circulant channel matrix $\boldsymbol{H} \in \mathbb{C}^{N\times N}$. Thus, a circulant channel matrix $\boldsymbol{H}$ is defined as

$$\boldsymbol{H} = \begin{bmatrix} h_0 & h_1 \dots & h_{N-1}\\ h_{N-1} & h_0 \dots & h_{N-2}\\ \vdots & \vdots \ \ \ddots & \vdots\\ h_1 & h_2 \dots & h_0 \end{bmatrix}, \tag{8}$$

where $h_{mn} = [\boldsymbol{H}]_{m,n} = h_{(n-m)_N}$, $(\kappa)_N$ denotes κ mod N, where mod stands for modulo operation, defined as $(\kappa)_N = \kappa \pm iN$, with i denoting an arbitrary integer number.

The eigenvalues and eigenvectors of circulant channel matrices are the solution to the system of linear equations

$$\boldsymbol{H}\boldsymbol{u}_l = \lambda_l\boldsymbol{u}_l. \tag{9}$$

The l^{th} eigenvalue of the circulant channel matrix $\boldsymbol{H}$ is defined as [15]

$$\lambda_l = \sum_{k=0}^{N-1} h_k e^{-j\frac{2\pi kl}{N}}, \tag{10}$$

which is the un-normalized DFT of the first row of the circulant channel matrix $\boldsymbol{H}$, while the l^{th} eigenvector of the circulant matrix $\boldsymbol{H}$ (all circulant matrices share the same eigenvectors) is given by

$$\boldsymbol{u}_l = \boldsymbol{f}_l = \frac{1}{\sqrt{N}}\left[1 \ \ e^{-j\frac{2\pi l}{N}} \ \ \dots \ \ e^{-j\frac{2\pi(N-1)l}{N}}\right]^T. \tag{11}$$

Therefore, from (9)–(11), the eigenvalue decomposition of the circulant channel matrix $\boldsymbol{H}$ is written as

$$\begin{aligned}\boldsymbol{H} &= \boldsymbol{U}\boldsymbol{\Sigma}\boldsymbol{U}^{\dagger}\\ &= \sqrt{N}\boldsymbol{U}\text{diag}\left(\boldsymbol{U}\boldsymbol{h}\right)\boldsymbol{U}^{\dagger},\end{aligned} \tag{12}$$

where $\boldsymbol{U}$ is the eigenvectors matrix of $\boldsymbol{H}$, represented by an $N \times N$ unitary DFT matrix with entries $[\boldsymbol{U}]_{n,l} = \frac{1}{\sqrt{N}}e^{-j\frac{2\pi nl}{N}}$, $n, l = 0, \dots, N-1$, while the eigenvalues of $\boldsymbol{H}$ are defined as $\boldsymbol{\Sigma} = \sqrt{N}\text{diag}(\boldsymbol{U}\boldsymbol{h})$, which could also be represented based on (10) as $\boldsymbol{\Sigma} = \text{diag}(\lambda_0, \dots \lambda_{N-1})$.

Therefore, from (12), in order to diagonalize the OAM channel, the transmit and receive PSNs must be perfectly aligned to the eigenvectors matrix of the OAM channel. This is due to the fact that OAM mode offset between the transmit and receive PSNs destroys the orthogonality between different modes, thus, resulting in IMI which severely deteriorates the spectral efficiency of the system. Hence, in the next section, the impact of constant OAM mode offset on the spectral efficiency of the system is rigorously investigated first, and subsequently, it is extended to the case of random OAM mode offset.

III. THE OVERALL SINR

In this section, an explicit closed-form expression for the SINR is derived for each OAM mode in the presence of OAM mode offset in the network of phase shifters at the receiver. In order to do that, we first derive the received signal before the network of phase shifters in the following Proposition.

Proposition 1: The received signal at the m^{th} receive antenna (before the analog combiner) can be represented as

$$r_m = \frac{1}{\sqrt{N}}\sum_{l=0}^{M-1}\sqrt{p_l}\lambda_l s_l e^{-j\frac{2\pi ml}{N}} + n_m, \tag{13}$$

where λ_l is the l^{th} OAM mode eigenvalue of the circulant channel matrix $\boldsymbol{H}$ whose entries are defined in (10).

Proof: The proof is given in Appendix A. ■

In order to recover the transmitted OAM signal, an N element receive UCA antenna connected with a network of fixed phase shifters and OAM mode selection is utilized at the receiver. In the presence of mismatch between the activated OAM modes at the transmit DFT and receive IDFT matrices,[3] i.e., when the transmit and receive PSNs have a constant OAM mode offset of ϵ, the negative effect of OAM mode offset on the SINR is analyzed herein. In order to do that, we derive the received OAM signal after the network of phase shifters at the receiver in the following Proposition.

Proposition 2: In the presence of OAM mode offset of ϵ at the receive PSN, the recovered p^{th} OAM mode signal (after the analog combiner) can be derived as

$$y_p = \sqrt{p_p}\lambda_p s_p c\left(p,\, p\right) + \sum_{\substack{l=0\\ l\neq p}}^{M-1} \sqrt{p_l}\lambda_l s_l c\left(l,\, p\right) + \widetilde{n}_p, \qquad (14)$$

where $c(l,\, p) = \frac{\text{sinc}(p-l+\epsilon)}{\text{sinc}(\frac{1}{N}(p-l+\epsilon))} e^{j\frac{\pi}{N}(p-l+\epsilon)(N-1)}$, with $\text{sinc}(x) = \frac{\sin(\pi x)}{\pi x}$,

and the AWGN $\widetilde{n}_p = \frac{1}{\sqrt{N}}\sum_{m=0}^{N-1} n_m e^{j\frac{2\pi(p+\epsilon)m}{N}}$ is the IDFT of the received AWGN $n_m,\ m = 0,\, \ldots,\, N-1$. Due to the unitary property of the IDFT transform, $\widetilde{n}_p$ has the same statistical distribution as n_m, i.e., $\widetilde{n}_p \sim \mathcal{CN}(0,\, \sigma^2)$.

Proof: The proof is given in Appendix B. ■

A. Key Observations:

First of all, let the OAM mode offset ϵ in (14) be represented by a sum of an integer and fractional parts, as follows $\epsilon = k + \varepsilon$, where k is an integer and $|\varepsilon| \leq 0.5$. If $|\epsilon| > 1$, the desired p^{th} mode signal will be received by the $(p+k)^{\text{th}}$ mode receiver instead. Therefore, in order to avoid such scenario, it is assumed here that $k = 0$.

OAM mode orthogonality is achieved in the IMI free case, i.e., when $\epsilon = 0$. In this case, $c(l,\, p) = \delta[(p-l)_N]$, where $\delta[\cdot]$ denotes the Dirac delta function. Hence, in this case, equation (14) reduces to $y_p = \sqrt{p_p}\lambda_p s_p + \widetilde{n}_p$. Therefore, in a matrix format, based on the eigenvalue decomposition of the circulant channel matrix in (4), the received signal before the analog IDFT combiner is given by

$$\begin{aligned} \boldsymbol{r} &= \boldsymbol{HFPs} + \boldsymbol{n} \\ &= \sqrt{N}\boldsymbol{F}\text{diag}\left(\boldsymbol{Fh}\right)\boldsymbol{Ps} + \boldsymbol{n}. \end{aligned} \qquad (15)$$

Hence, in the absence of OAM mode offset at the receiver, i.e., when the receive IDFT combiner matrix is given by $\boldsymbol{W}^\dagger = \boldsymbol{F}^\dagger$, the received OAM signal vector after the combiner is diagonalized as follows

$$\begin{aligned} \boldsymbol{y} &= \boldsymbol{W}^\dagger \boldsymbol{r} \\ &= \sqrt{N}\text{diag}\left(\boldsymbol{Fh}\right)\boldsymbol{Ps} + \boldsymbol{F}^\dagger \boldsymbol{n}. \end{aligned} \qquad (16)$$

On the other hand, in the presence of OAM mode offset at the receiver, the desired p^{th} mode signal $\lambda_p\sqrt{p_p}s_p$ is not only attenuated by $|c(p,\, p)| = |\frac{\text{sinc}(\epsilon)}{\text{sinc}(\frac{\epsilon}{N})}|$, but it is also subject to IMI due to the OAM mode offset at the receiver.

Based on (14), assuming a one tap equalizer and perfect free-space channel state information (CSI) at the receiver, the desired p^{th} mode signal decision variable is given as

$$\widehat{s_p} = s_p + \frac{\sum_{\substack{l=0\\ l\neq p}}^{M-1} \sqrt{p_l}\lambda_l s_l c\left(l,\, p\right) + \widetilde{n}_p}{\sqrt{p_p}\lambda_p c\left(p,\, p\right)}. \qquad (17)$$

Conditioned on $\boldsymbol{h}$ and ϵ, the IMI term $\sum_{\substack{l=0\\ l\neq p}}^{M-1} \sqrt{p_l}\lambda_l s_l c(l,\, p)$ is represented by a complex circular symmetric Gaussian random variable with zero mean and variance of $\sum_{\substack{l=0\\ l\neq p}}^{M-1} p_l|\lambda_l|^2|c(l,\, p)|^2$, whereas the AWGN $\widetilde{n}_p \sim \mathcal{CN}(0,\, \sigma^2)$ is independent of the IMI. Therefore, the SINR for the p^{th} OAM mode signal is written as

$$\text{SINR}_p = \frac{\rho_p\left|\lambda_p\right|^2\left|c\left(p,\, p\right)\right|^2}{1 + \sum_{\substack{l=0\\ l\neq p}}^{M-1} \rho_l\left|\lambda_l\right|^2\left|c\left(l,\, p\right)\right|^2}, \qquad (18)$$

where $\rho_p = \frac{p_p}{\sigma^2}$ is the signal-to-noise ratio (SNR) for the p^{th} OAM mode signal.

Thus, the achievable spectral efficiency of the MDM-OAM system is expressed as

$$\mathcal{R} = \sum_{p=0}^{M-1} \mathcal{R}_p = \sum_{p=0}^{M-1} \log_2\left(1 + \text{SINR}_p\right). \qquad (19)$$

B. Random OAM Mode Offset

In this subsection, we investigate the impact of random OAM mode offset on the spectral efficiency of MDM-OAM systems. In contrast to (14) where a fixed OAM mode offset is considered for all OAM modes, in this subsection, the OAM mode offset between the the p^{th} OAM mode and l^{th} OAM mode $\epsilon_{p,\, l}$ is considered to be different and randomly distributed according to a predefined probability density function. Two commonly used assumptions are leveraged here (see e.g., [21]), where the OAM mode offset is assumed uniformly distributed according to $\epsilon_{p,\, l} \sim \mathcal{U}(\epsilon_{\min},\, \epsilon_{\max})$, or distributed according to a Gaussian distribution according to $\epsilon_{p,\, l} \sim \mathcal{N}(0,\, \sigma_\epsilon^2)$. For a fair comparison between the investigated uniform and Gaussian distribution models, we set the variance of both distributions to $\sigma_\epsilon^2 = \frac{(\epsilon_{\max} - \epsilon_{\min})^2}{12}$.

In the presence of a random OAM mode offset of $\epsilon_{p,\, l}$ at the receive PSN, and by following similar derivations to (42), the received p^{th} OAM mode signal can be written as

$$\begin{aligned} y_p &= \frac{1}{\sqrt{N}}\sum_{m=0}^{N-1} r_m e^{j\frac{2\pi\left(p+\epsilon_{p,\, l}\right)m}{N}} \\ &= \sqrt{p_p}\lambda_p s_p c\left(p,\, p\right) + \sum_{\substack{l=0\\ l\neq p}}^{M-1} \sqrt{p_l}\lambda_l s_l c\left(l,\, p\right) + \widetilde{n}_p, \end{aligned} \qquad (20)$$

where $c(l,\, p) = \frac{\text{sinc}(p-l+\epsilon_{p,\, l})}{\text{sinc}(\frac{1}{N}(p-l+\epsilon_{p,\, l}))} e^{j\frac{\pi}{N}(p-l+\epsilon_{p,\, l})(N-1)}$. Hence, in this case, the achievable spectral efficiency of random OAM mode offset is expressed as

$$\mathcal{R} = \sum_{p=0}^{M-1} \mathbb{E}\left[\log_2\left(1 + \text{SINR}_p\right)\right], \qquad (21)$$

---

[3] For instance, consider the transmitted OAM signal excited with an OAM mode l_t that is given as $s_{l_t}e^{jl_t\varphi}$. Therefore, in order to recover this OAM signal, the receiver excites an OAM mode l_r, that tries to be synchronized with the transmit OAM mode l_t. However, due the existence of synchronization errors, the receiver excites the OAM mode l_r as $l_r = l_t + \epsilon$.

where the expectation is over the OAM mode offset distribution. The SINR_p given in (21) is defined similarly to that in (18) with $c(l, p)$ given in (20).

For a simpler evaluation of (21), Jensen's inequality, through the concavity of the function $f(x) = \log_2(x),\ \forall\, x \geq 0$ and the convexity of the function $g(y) = \frac{1}{y},\ \forall\, y \geq 0$, could be leveraged to get a simpler approximation derived in (22), shown at the bottom of this page,

where $\mathbb{E}[|c(l, p)|^2] = \frac{1}{N^2}\int_{-\infty}^{\infty} \frac{\sin^2(\pi(p-l+\epsilon))}{\sin^2(\frac{\pi}{N}(p-l+\epsilon))} f_{\epsilon_{p,l}}(\epsilon) d\epsilon$,[4] and $f_{\epsilon_{p,l}}(\epsilon)$ is the probability density function of the OAM mode offset $\epsilon_{p,l}$.

IV. OAM MODE SELECTION SCHEME

In the previous section, the activated OAM modes have been chosen arbitrarily based on $\boldsymbol{F}$, i.e., the OAM mode selection network was chosen in a fixed manner, where the first M OAM modes were activated blindly (i.e. regardless of the channel quality associated with the activated OAM modes) according to $l \in \{0,\ 1,\ \ldots,\ M-1\}$. However, such an OAM mode activation scheme does not result in the best possible spectral efficiency performance, as the channel quality information is ignored. Hence, in this section, we propose a new optimal OAM mode selection scheme that activates the OAM modes corresponding to the strongest M OAM channel eigenmodes. First, let us denote the index set of the activated OAM modes as $\mathcal{S} = \{\pi(1),\ \pi(2),\ \ldots,\ \pi(M)\}$, where $\pi(i)$ is the index of the i^{th} activated mode. Note that we have fixed DFT eigendirection candidates at the transmitter, given by $\mathcal{F} = \{\boldsymbol{f}_0,\ \boldsymbol{f}_1,\ \ldots,\ \boldsymbol{f}_{N-1}\}$, where $\boldsymbol{f}_l$ is defined after (4). Similarly, fixed IDFT eigendirection candidates are present at the receiver, defined as $\mathcal{W} = \{\boldsymbol{w}_0,\ \boldsymbol{w}_1,\ \ldots,\ \boldsymbol{w}_{N-1}\}$, where $\boldsymbol{w}_l$ is defined after (4). Given that $\mathcal{F}$ and $\mathcal{W}$ comprises N OAM mode candidates, only M OAM modes corresponding to the strongest eigendirections are activated through mode training phase. In the absence of CSI at the receiver,[5] the transmitter transmits N OAM modes as training symbols and sequentially sweeps through all N eigendirections of the codebook in $\mathcal{F}$, while the receiver sweeps through all N eigendirections of the codebook in $\mathcal{W}$ by following the same transmit beam index candidate, thereby, requiring a complexity cost of only $O(N)$. Therefore, the index for the l^{th} activated OAM mode $\pi(l)$ is defined as[6]

$$\pi(l) = \underset{\boldsymbol{f}_l \in \mathcal{F}\ \boldsymbol{w}_l \in \mathcal{W}}{\arg\max} \left| \boldsymbol{w}_l^{\dagger} \boldsymbol{H} \boldsymbol{f}_l \right|. \tag{23}$$

Note that this mode activation training and mode selection is performed at the receiver, thus, no CSIT is required. The activated OAM mode indices $\mathcal{S} = \{\pi(1),\ \pi(2),\ \ldots,\ \pi(M)\}$ are then fed back to the transmitter via a low rate feedback channel to be selected from the transmit analog DFT precoder for OAM signal transmission, i.e., $\boldsymbol{F} = [\boldsymbol{f}_{\pi(1)}\ \boldsymbol{f}_{\pi(2)}\ \cdots\ \boldsymbol{f}_{\pi(M)}]$. Similarly, the activated receive analog IDFT combiner for OAM signal recovery is given as $\boldsymbol{W} = [\boldsymbol{w}_{\pi(1)}\ \boldsymbol{w}_{\pi(2)}\ \ldots\ \boldsymbol{w}_{\pi(M)}]$. The feedback overhead required for feeding back one OAM mode index $\pi(l)$ from the receiver to the transmitter is given by $B = \log_2(N)$ bits.

Therefore, in the presence of OAM mode selection network, the received signal at the m^{th} receive antenna before combiner is given by[7]

$$r_m = \frac{1}{\sqrt{N}} \sum_{l \in \mathcal{S}} \sqrt{p_l} \lambda_l s_l e^{-j\frac{2\pi m l}{N}} + n_m. \tag{24}$$

Now, the recovered p^{th} activated OAM mode signal, $p \in \mathcal{S}$ after the combiner can be written as

$$y_p = \sqrt{p_p} \lambda_p s_p c\,(p,\, p) + \sum_{l \in \mathcal{S},\, l \neq p} \sqrt{p_l} \lambda_l s_l c\,(l,\, p) + \widetilde{n}_p. \tag{25}$$

Thus, the SINR for the p^{th} activated OAM mode is written by

$$\mathrm{SINR}_p = \frac{\rho_p \left|\lambda_p\right|^2 \left|c\,(p,\, p)\right|^2}{1 + \sum_{l \in \mathcal{S},\, l \neq p} \rho_l \left|\lambda_l\right|^2 \left|c\,(l,\, p)\right|^2}. \tag{26}$$

$$\begin{aligned}
\mathcal{R} &\leq \sum_{p=0}^{M-1} \log_2 \left(1 + \mathbb{E}\left[\frac{\rho_p \left|\lambda_p\right|^2 \left|c\,(p,\, p)\right|^2}{1 + \sum_{\substack{l=0 \\ l \neq p}}^{M-1} \rho_l \left|\lambda_l\right|^2 \left|c\,(l,\, p)\right|^2} \right] \right) \\
&= \sum_{p=0}^{M-1} \log_2 \left(1 + \mathbb{E}\left[\rho_p \left|\lambda_p\right|^2 \left|c\,(p,\, p)\right|^2 \right] \mathbb{E}\left[\frac{1}{1 + \sum_{\substack{l=0 \\ l \neq p}}^{M-1} \rho_l \left|\lambda_l\right|^2 \left|c\,(l,\, p)\right|^2} \right] \right) \\
&\geq \sum_{p=0}^{M-1} \log_2 \left(1 + \frac{\rho_p \left|\lambda_p\right|^2 \mathbb{E}\left[\left|c\,(p,\, p)\right|^2 \right]}{1 + \sum_{\substack{l=0 \\ l \neq p}}^{M-1} \rho_l \left|\lambda_l\right|^2 \mathbb{E}\left[\left|c\,(l,\, p)\right|^2 \right]} \right),
\end{aligned} \tag{22}$$

---

[4] Note that this integral, though not amenable to a closed-form expression, can be numerically solved using any standard software packages (e.g. MATLAB, Mathematica).

[5] Note that, alternatively, in order to find the OAM mode which results in the maximum SINR, perfect knowledge of the SNR, OAM mode offset, and the circulant channel matrix $\boldsymbol{H}$ need to be available at the receiver.

[6] In the presence of full CSI of the OAM channel $\boldsymbol{H}$ at the receiver and absence of OAM mode offset, where the eigenvalues of $\boldsymbol{H}$ are given by $\boldsymbol{\Sigma} = \sqrt{N}\mathrm{diag}(\boldsymbol{U}\boldsymbol{h})$, the optimal OAM mode selection scheme could alternatively be written as $\pi(l) = \underset{\boldsymbol{u}_l \in \mathcal{U}}{\arg\max}\ |\boldsymbol{u}_l^T \boldsymbol{h}|$, where $\mathcal{U} = \{\boldsymbol{u}_0,\ \boldsymbol{u}_1,\ \ldots,\ \boldsymbol{u}_{N-1}\}$.

[7] Note that here the only difference between equations (13)–(14), (18)–(19) and the upcoming equations (24)–(27) is that the latter use the optimal mode selection scheme defined in (23).

Hence, the achievable spectral efficiency of the system in (19) is modified as

$$\mathcal{R}(\mathcal{S}) = \sum_{l \in \mathcal{S}} \log_2 \left(1 + \mathrm{SINR}_l\right). \tag{27}$$

V. ZERO-FORCING RECEIVER

In order to alleviate the negative impact of OAM offset on the performance of the system, a digital baseband precoding stage is embedded at the receiver. In the hybrid analog and digital precoding structure, it is difficult to acquire full CSI of the entire channel matrix through all antenna elements. This is because a high number of antenna elements are connected to a much less number of RF chains through a fixed phase shifting network. More specifically, since the channel estimator in the digital baseband pinpoints only to a reduced dimensionality channel through the fewer number of RF chains, it is infeasible to acquire the entire channel $\boldsymbol{H}$ at the receiver. Therefore, the received OAM signal vector before the augmented digital baseband precoder $\boldsymbol{G}$ is given as

$$\begin{aligned} \boldsymbol{y} &= \boldsymbol{W}^{\dagger} \boldsymbol{H} \boldsymbol{F} \boldsymbol{P} \boldsymbol{s} + \boldsymbol{n} \\ &= \sqrt{N} \boldsymbol{W}^{\dagger} \boldsymbol{F} \mathrm{diag}\left(\boldsymbol{F} \boldsymbol{h}\right) \boldsymbol{P} \boldsymbol{s} + \boldsymbol{n}. \end{aligned} \tag{28}$$

Let the effective channel seen by the digital baseband at the receiver be given by $\boldsymbol{H}_{\text{eff}} = \boldsymbol{W}^{\dagger} \boldsymbol{H} \boldsymbol{F}$. Then, a ZF precoder can be designed at the receiver to completely eliminate the severe inter-channel interference caused by the OAM offset between the transceivers phase shifting networks. However, this can be done only under the knowledge of accurate CSI of $\boldsymbol{H}_{\text{eff}}$ at the receiver.[8] Therefore, conditioned on $\boldsymbol{H}_{\text{eff}}$, the ZF precoder[9] is given as $\boldsymbol{G} = \boldsymbol{H}_{\text{eff}}^{+} = (\boldsymbol{H}_{\text{eff}}^{\dagger} \boldsymbol{H}_{\text{eff}})^{-1} \boldsymbol{H}_{\text{eff}}^{\dagger}$. Hence, the received OAM signals after the augmented digital ZF precoder is given

$$\begin{aligned} \boldsymbol{z} &= \boldsymbol{G} \boldsymbol{y} \\ &= \boldsymbol{P} \boldsymbol{s} + \boldsymbol{G} \boldsymbol{n}. \end{aligned} \tag{29}$$

Therefore, in the presence of a digital ZF precoder $\boldsymbol{G}$ at the receiver, the SINR for the p^{th} OAM mode signal is given by

$$\mathrm{SINR}_p^{\mathrm{ZF}} = \frac{\rho_p}{\left[\left(\boldsymbol{H}_{\text{eff}}^{\dagger} \boldsymbol{H}_{\text{eff}}\right)^{-1}\right]_{p,p}} \tag{30}$$

$$= \rho_p \left\| \boldsymbol{B}_p^{\perp} \boldsymbol{h}_{\text{eff},\,p} \right\|^2, \tag{31}$$

where $\boldsymbol{B}_p^{\perp} = \boldsymbol{I}_M - \boldsymbol{H}_{\text{eff},\,p} (\boldsymbol{H}_{\text{eff},\,p}^{\dagger} \boldsymbol{H}_{\text{eff},\,p})^{-1} \boldsymbol{H}_{\text{eff},\,p}^{\dagger}$ is the null space projection matrix of the effective channel $\boldsymbol{H}_{\text{eff}}$, $\boldsymbol{H}_{\text{eff},\,p}$ is the effective channel matrix which excludes $\boldsymbol{h}_{\text{eff},\,p}$, and $\boldsymbol{h}_{\text{eff},\,p}$ is the p^{th} column of $\boldsymbol{H}_{\text{eff}}$.

VI. EXPERIMENTAL RESULTS

In order to verify the introduced theoretical OAM system performance, we performed practical experimentation on an OAM circular antenna array. The array unit cell is designed using microstrip patch antenna technology having dimensions of 20 × 13.4 mm^2, fed by a coaxial at 3.10 mm inside the patch broader. The unit cell dimensions are 13.20 × 20 mm^2. The circular antenna array is designed by replicating $N = 9$ unit cells in a circle with diameter around 105 mm. The circular antenna is designed to operate at 5.8 GHz and is developed on Rogers $RO4003C$ substrate sheet having dimensions 274.00 × 198.00 × 0.51 mm^3. The electrical properties of the substrate are a dielectric constant of $\epsilon_r = 3.38$ and a loss tangent of $\tan\delta = 0.0027$.

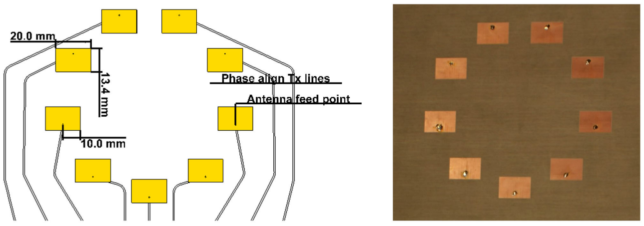

(a) (b)

Fig. 2. (a) Geometric dimensions of the microstrip patch antennas of the OAM circular array. (b) Fabricated circular antenna array developed on Taconic RF-60 substrate. The antenna array is connected to a Rotman lens based feed network that is capable of generating 5 OAM radiation modes.

The OAM transmitter generally requires a feed network connected to the antenna array to generate the phase ramp required to create the composite transmitted signal x_n from equation (2) [17], [18], [25]. The mode generation and selection in our circular antenna array is controlled by a Rotman lens based feed network having 9 array ports and 5 beam ports.[10] Each array port of the Rotman lens is separately connected to one antenna unit cell in the circular antenna array via phase aligned transmission lines. The Rotman lens has 5 beam ports which corresponds to its capability of generating 5 spatially orthogonal OAM transmission modes [26], [27] at 5.8 GHz. The Rotman lens is designed and tested on Taconic RF-60 substrate having dimensions 477.00 × 198.00 × 0.64 mm^3 with dielectric constant of $\epsilon_r = 6.15$ and loss tangent of $\tan\delta = 0.0038$. The Rotman lens design parameters include on-axis focal length of 4.5λ, ratio between on-and off-axis focal lengths of 0.88, focal angle of 30° and lens expansion factor of 0.9. The definition of Rotman lens design parameters can be found in [28]. In order to verify the introduced theoretical OAM system framework, we implement a practical experimentation on an OAM circular antenna array designed using the synthesis provided in [29]–[32].

The circular array and the Rotman lens were fabricated using milling machine model LPKF Protomate H100, while the field patterns were carried out in NSI near-field Anechoic chamber. The antenna configuration and array formulation are shown in Fig. 2. The circular antenna array was placed in the anechoic chamber and a 5.8 GHz signal was excited via each array port corresponding to each OAM mode. A 5.8 GHz measurement

---

[8] Grid of beams (beam sweeping) codebook or compressed sensing techniques could be used for channel estimation at the receiver [22]–[24].

[9] Note that a pseudo-inverse is used here for generality. This is because when $\boldsymbol{H}_{\text{eff}}$ is a square matrix (which is the case considered in this work), $\boldsymbol{H}_{\text{eff}}^{+} = \boldsymbol{H}_{\text{eff}}^{-1}$.

[10] Although in this investigation we use Rotman lens as RF PSN, note that the proposed model is suitable for any PSN architecture that includes active phase shifters, Fourier lens, Butler matrix and delay lines. Since the mode offset is hardware specific, correlation between modes will be different for each network hardware.

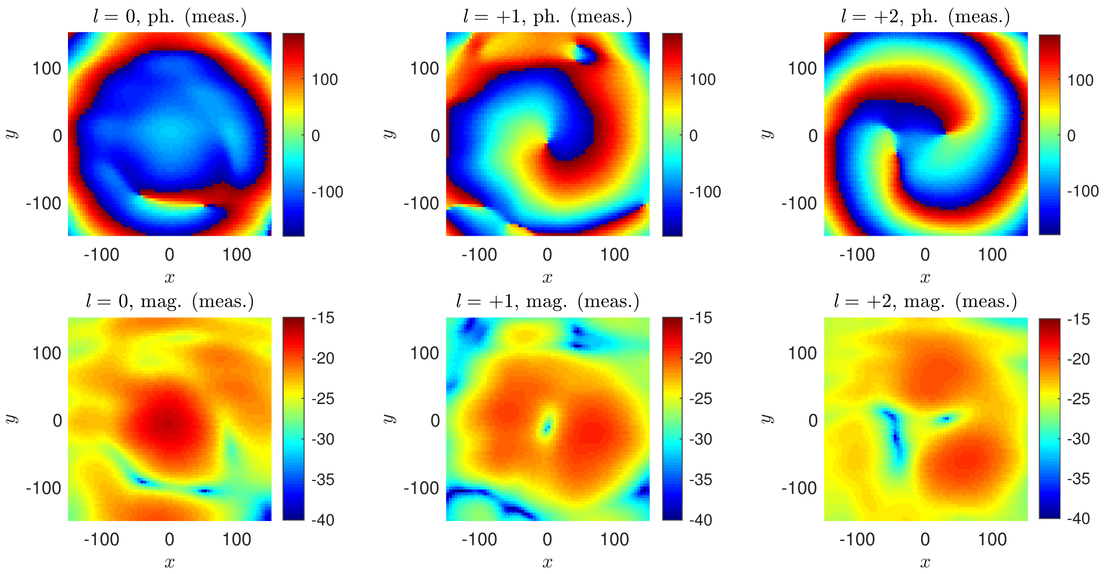

Fig. 3. Measured phase and magnitude co-polarized field patterns against three OAM radiation modes i.e. $l = 0, +1$ and $+2$.

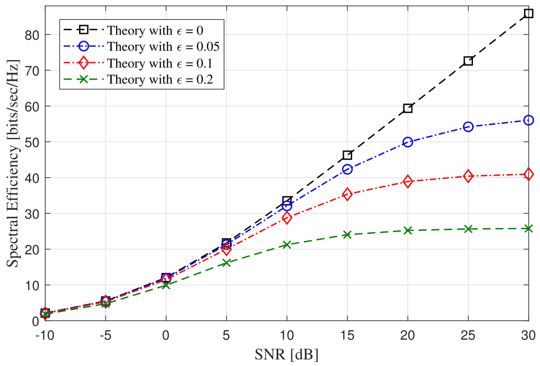

Fig. 4. The spectral efficiency versus the SNR.

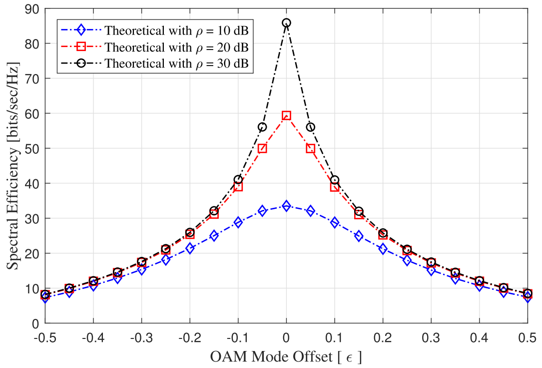

Fig. 5. The spectral efficiency versus the OAM mode offset ϵ.

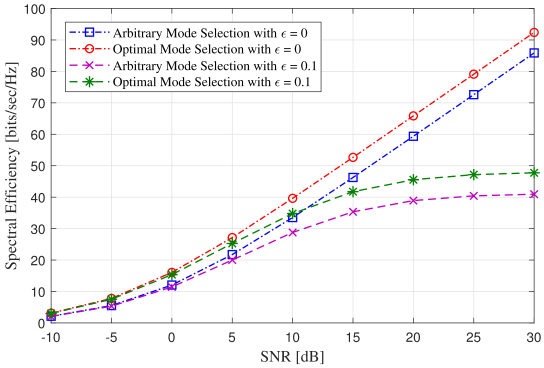

Fig. 6. The spectral efficiency versus the SNR for the optimal OAM mode selection scheme.

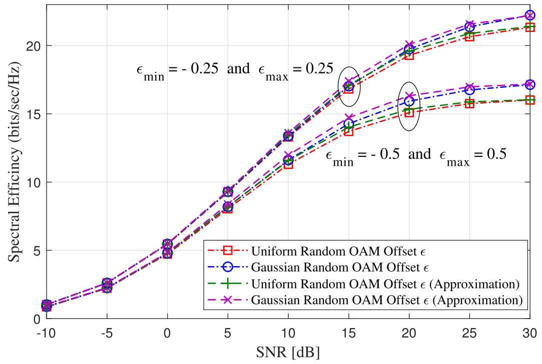

Fig. 7. The spectral efficiency of random OAM mode offset versus the SNR for modes $-2, 0, +2$.

probe was used to scan a near-field plane in-front of the antenna array, which recorded the complex electric field values. The measured field patterns are presented in Fig. 3, in which the magnitude and the phase of the electric field are given. The magnitude for $l = 0$ shows a directive beam pattern, while for mode $l = +1$ and $+2$, shows vortex beams, both of them matching well with the simulation predictions. The phase values of the measured electric field represents one cycle of phase spiral for $l = +1$ and two cycles for $l = +2$. Far-field patterns are mathematically evaluated using the measured data by the method given in [33]. The field patterns in Fig. 3 are close to

TABLE I
THE MAGNITUDE OF MEASUREMENT OAM MODE CORRELATIONS

	-2	-1	0	$+1$	$+2$
-2	1	0.4642	0.0828	0.1898	0.1805
-1	0.4642	1	0.2654	0.4340	0.1898
0	0.0828	0.2654	1	0.1383	0.1289
$+1$	0.1898	0.4340	0.1383	1	0.4642
$+2$	0.1805	0.1898	0.1289	0.4642	1

the predictions given in the wealth of the OAM literature in [34] and references therein. The non-uniform field intensity for the modes $l = +1$ and $+2$ are due to fabrication anomalies. We consider this measurement data for our further calculation in an attempt to analyze practical specification. The mode $l = 0$ results in a directive beam with almost uniform phase difference along the boresight direction. For the modes $l = +1$ and $+2$, directive beams are noticeable with a null along the broadsight. A single phase spiral cycle of $0^\circ - 360^\circ$ and a double phase spiral is evident from the phase plots for the modes $l = +1$ and $+2$, respectively.

A. Similarity Measure

In order to support our theoretical OAM analysis, OAM measurements have been conducted. To accurately approximate the OAM mode offset of the experiment, a similarity measure metric is used between the analytical and measured magnitude of correlation matrices. Due to the hardware limitations, the conducted measurement is expected to have different system imperfections. However, only the OAM mode offset is considered in the theoretical analysis. The correlation matrix distance (CMD) is used to measure the distance between the analytical and measurement correlation matrices' magnitude, $\boldsymbol{R}_1$ and $\boldsymbol{R}_2$ respectively. Thus, the CMD is defined as [35]

$$d_{\text{corr}}\left(\boldsymbol{R}_1,\ \boldsymbol{R}_2\right) = 1 - \frac{\operatorname{Tr}\left(\boldsymbol{R}_1 \boldsymbol{R}_2\right)}{\left\|\boldsymbol{R}_1\right\|_F \left\|\boldsymbol{R}_2\right\|_F}. \tag{32}$$

For instance, $d_{\text{corr}}(\boldsymbol{R}_1,\ \boldsymbol{R}_2) = 0$ means that $\boldsymbol{R}_1 = \boldsymbol{R}_2$, whereas $d_{\text{corr}}(\boldsymbol{R}_1,\ \boldsymbol{R}_2) = 1$ means that $\boldsymbol{R}_1$ and $\boldsymbol{R}_2$ are completely different. The magnitude of the theoretical OAM mode correlation matrix entries are given by $[\boldsymbol{R}_1]_{m,\,n} = |c(m,\ n)|$, where $c(m,\ n)$ is given in (14), whereas the magnitude of the measurement OAM mode correlation matrix $\boldsymbol{R}_2$ entries are given in Table I.

VII. NUMERICAL RESULTS

A. Theoretical Results

In this section, a set of numerical results are provided to evaluate the spectral efficiency performance in the presence of OAM mode offset. For ease of exposition, the power is equally allocated amongst different OAM modes, i.e., $\boldsymbol{P} = \sqrt{\frac{P}{M}}\boldsymbol{I}_N$, thus $\rho_l = \rho = \frac{P}{M\sigma^2}\ \forall\, l \in \mathcal{S}$. In our simulations, the channel gain in (6) is normalized such that $\beta\frac{\lambda}{4\pi d_{mn}} = 1$ (except for Fig. 8). Unless otherwise stated, the system settings for Figs. 4–6 are chosen as follows, $N = 16$, $M = 8$, $\lambda = 0.05$, $D = 10\lambda$, and $R_T = R_R = 0.6$.

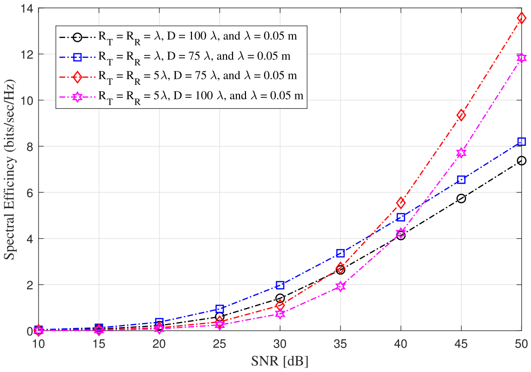

Fig. 8. The spectral efficiency versus the SNR for modes -2, 0, $+2$, with $N = 9$, $M = 3$, $\lambda = 0.05\,m$, $\beta = 10$, and $\epsilon = 0.1$.

Fig. 4 shows the spectral efficiency versus the SNR for different values of constant OAM mode offset ϵ. It is clearly seen that the spectral efficiency degradation increases as the OAM mode offset increases, and also as the SNR increases. This is not only due to the useful received signal attenuation, which is proportional to the OAM mode offset, according to $|c(p,\ p)| = |\frac{\operatorname{sinc}(\epsilon)}{\operatorname{sinc}(\frac{\epsilon}{N})}|$ in (18), but also due to the increase in IMI through $|c(l,\ p)| = |\frac{\operatorname{sinc}(p-l+\epsilon)}{\operatorname{sinc}(\frac{1}{N}(p-l+\epsilon))}|$. As the SNR increases, the spectral efficiency degradation becomes stronger since the IMI is linearly proportional to the SNR ρ through $\sum_{\substack{l=0 \\ l\neq p}}^{M-1} \rho|\lambda_l|^2|c(l,\ p)|^2$ in (18).

In Fig. 5, the spectral efficiency versus the OAM mode offset ϵ is presented for multiple SNR values. The negative impact of the OAM mode offset on the spectral efficiency is clearly observed. It can be seen that the spectral efficiency deterioration due to OAM mode offset is stronger at high SNR.

Fig. 6 shows the positive impact of the optimal OAM mode selection scheme on the spectral efficiency of the system. The analog DFT precoder and IDFT combiner based on the arbitrary OAM mode selection scheme are respectively given by $\boldsymbol{F} = [\boldsymbol{f}_0\ \boldsymbol{f}_1\ \ldots\ \boldsymbol{f}_{M-1}]$ and $\boldsymbol{W} = [\boldsymbol{w}_0\ \boldsymbol{w}_1\ \ldots\ \boldsymbol{w}_{M-1}]$, whereas the analog DFT precoder and IDFT combiner based on the optimal OAM mode selection scheme introduced in (23) are respectively given as $\boldsymbol{F} = [\boldsymbol{f}_{\pi(1)}\ \boldsymbol{f}_{\pi(2)}\ \cdots\ \boldsymbol{f}_{\pi(M)}]$ and $\boldsymbol{W} = [\boldsymbol{w}_{\pi(1)}\ \boldsymbol{w}_{\pi(2)}\ \ldots\ \boldsymbol{w}_{\pi(M)}]$. Obviously, activating the OAM modes which correspond to the dominant OAM eigenmodes of the channel, results in consistently better spectral efficiency performance.

In Fig. 7, the spectral efficiency of random OAM mode offset versus the SNR is presented. The system settings are chosen as follows: $N = 9$, $M = 3$, with activated OAM modes -2, 0, $+2$. Two scenarios are considered for the random OAM mode offset $\epsilon_{p,\,l}$: the uniform and Gaussian random variable distributions, and distributed according to $\epsilon_{p,\,l} \sim \mathcal{U}(\epsilon_{\min},\ \epsilon_{\max})$ and $\epsilon_{p,\,l} \sim \mathcal{N}(0,\ \sigma_\epsilon^2)$ respectively, with $\sigma_\epsilon^2 = \frac{(\epsilon_{\max}-\epsilon_{\min})^2}{12}$. In addition, a simpler spectral efficiency approximation is also shown based on (22). The negative impact of OAM mode offset variance σ_ϵ^2 on the spectral efficiency performance is clearly seen in Fig. 7, and the tightness of the approximation is also apparent.

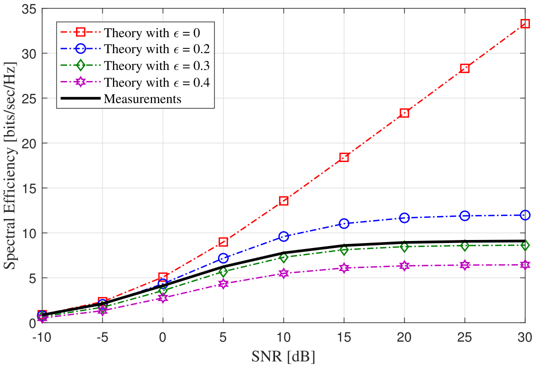

Fig. 9. The spectral efficiency versus the SNR for modes $0, +1, +2$.

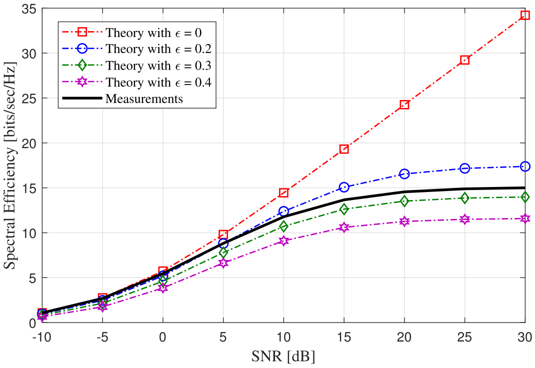

Fig. 10. The spectral efficiency versus the SNR for modes $-2, 0, +2$.

Fig. 8 shows the impact of the transmit and receive UCAs radii and the transmit and receive UCAs distance on the spectral efficiency performance. This is in contrast to the system settings chosen for Figs. 4–7, and takes into account the large scale fading pathloss effect through the OAM channel introduced in (6). As expected, a spectral efficiency degradation is observed when the distance between the transmit and receive UCAs increases. In addition, the transmit and receive UCAs radii have a critical impact on the spectral efficiency performance. For instance, at low to medium SNRs, small transmit and receive UCAs' radii result in a better spectral efficiency performance compared to a higher transmit and receive UCAs' radii. Ultimately, one can seek to jointly select the system parameters that achieve the highest possible spectral efficiency performance given a set of space constraints.

B. Comparison With Measurements

Figs. 9 –12 show the comparison between the theoretical analysis and measurement results. The system settings are chosen as follows, $N = 9$, $M = 3$. For comparison purposes, two activated mode settings have been investigated, a high mode separation case where mode $l = -2, 0, +2$ are selected, and a low mode separation case where mode $l = 0, +1, +2$ are selected. Three observations are made from the contour corresponding to the results in Figs. 9 and 10 for these two mode settings: First, the general trend of measurements matches well with the theoretical model given in the prior sections. Secondly, the spectral efficiency of mode setting $l = 0, +1, +2$ matches very well with the theoretical predictions for OAM mode offset of $\epsilon = 0.3$. Similarly, the case of mode setting $l = -2, 0, +2$ results in a spectral efficiency that matches very close to the theoretical contour for the OAM mode offset of $\epsilon = 0.3$. This confirms that mode separation has significant impact on the expected spectral efficiency, i.e., higher OAM mode separation results in higher spectral efficiency. For instance, at SNR $= 10$ dB, the spectral efficiency for OAM mode setting $l = -2, 0, +2$ is 12 bits/sec/Hz, whereas the spectral efficiency for OAM mode setting $l = 0, +1, +2$ is only 7 bits/sec/Hz.

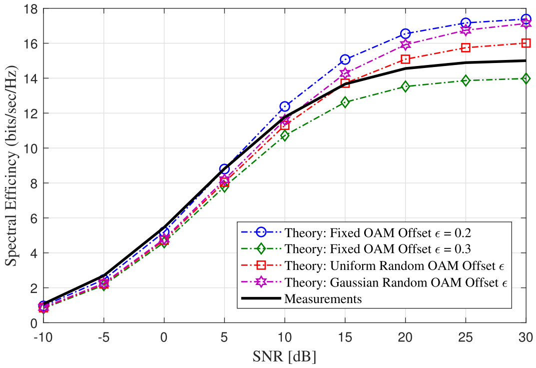

Fig. 11. The spectral efficiency of OAM mode offset versus the SNR for modes $-2, 0, +2$.

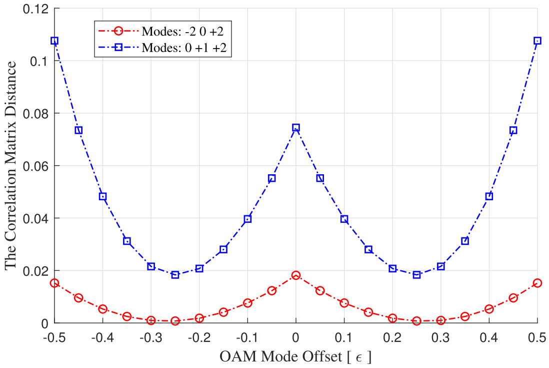

Fig. 12. The correlation matrix distance versus the OAM mode offset ϵ.

In Fig. 11, the case of random OAM mode offset is considered, where the spectral efficiency of random and constant OAM mode offset versus the SNR is presented for modes -2, 0, $+2$. In our theoretical simulations, we set $\epsilon_{\min} = -0.5$ and $\epsilon_{\max} = 0.5$. It is clearly seen that our practical measurement matches very well with the presented theoretical results with a uniform and Gaussian random OAM mode offset $\epsilon_{p,\,l}$, that is distributed according to $\epsilon_{p,\,l} \sim \mathcal{U}(\epsilon_{\min} = -0.5,\, \epsilon_{\max} = 0.5)$ and $\epsilon_{p,\,l} \sim \mathcal{N}(0,\, \sigma_{\epsilon}^2 = \frac{1}{12})$, respectively.

Fig. 12 presents the similarity measure metric of the correlation matrix distance to find the best approximations between the presented theoretical results and the practical measurements in the case of fixed OAM mode offset. It is observable that whichever mode combination is selected (mode setting $l = 0, +1, +2$ or mode setting $l = -2, 0, +2$), the least correlation matrix distance is expected to be at the OAM mode offset ranging from -0.3 to -0.2 and $+0.2$ to $+0.3$. Thus, the minimum distance $d_{\text{corr}}(\boldsymbol{R}_1,\, \boldsymbol{R}_2)$ is shown to occur approximately at $|\epsilon| = 0.25$. The OAM mode offset results in substantial spectral

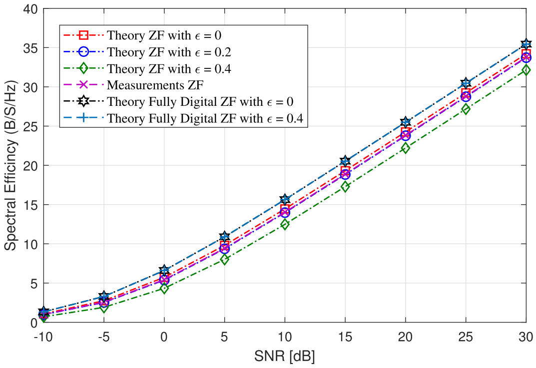

Fig. 13. The spectral efficiency versus the SNR for modes $-2, 0, +2$.

efficiency degradation. Therefore, for an optimal OAM system performance, an OAM mode offset estimation and compensation are indispensable at the receiver. Note that the selection of the least correlated modes for parallel data stream transmission over OAM radio is more likely an engineering problem, since practical mode distance (as generally defined in literature) does not always necessarily translate into low correlation. Correlation between the farthest modes can be highest and vice versa.

In Fig. 13, a substantial spectral efficiency performance improvement is shown compared to Figs. 4–11, thanks to the augmented reduced dimensionality baseband ZF scheme. The proposed low dimensional ZF combiner completely eliminates the negative impact of OAM mode offset at the receiver with marginal spectral efficiency loss when compared against its traditional fully digital ZF counterpart. However, the proposed ZF scheme comes at the cost of extra digital baseband processing stage at the receiver, in addition to the effective low dimensional channel estimation required for the ZF scheme. Furthermore, for comparison purposes, Fig. 13 includes the traditional fully digital ZF scheme where all OAM modes are activated. Although the traditional full complexity ZF precoder results in the highest spectral efficiency performance, as it perfectly eliminates the negative impact of OAM mode offset regardless of its severity, it incurs the highest cost and power consumption since N RF chains are required at the receiver, including the knowledge of full dimensional CSI of $\boldsymbol{H}_{\text{eff}} \in \mathbb{C}^{N \times N}$, which is a bottleneck in massive MIMO systems.

VIII. CONCLUSIONS

In the presence of OAM mode offset, this paper presented a unified closed-form SINR expression for each OAM mode, through which the spectral efficiency performance was investigated. In addition, in order to significantly improve the spectral efficiency of the system, a low-complexity optimal OAM mode selection scheme was proposed, where the OAM modes corresponding to the dominant eigendirections of the OAM channel were activated. Furthermore, an experiment demonstrating a 9×9 MDM-OAM communication link using OAM mode multiplexing was conducted at a microwave frequency of 5.8 GHz to support the theoretical analysis. The OAM mode offset attenuates the desired OAM mode signal and gives rise to inter-mode interference, which reduces the SINR, leading to the deterioration of the spectral efficiency performance. OAM mode offset results in spectral efficiency saturation as the SNR increases, i.e., the spectral efficiency performance saturates beyond a predefined SNR value. It is found that the spectral efficiency degradation increases monotonically as the OAM mode offset increases. In addition, the spectral efficiency degradation of a system operating at high SNR values is much worse than that of a system operating at low SNR values. Moreover, the investigated optimal OAM mode selection scheme resulted in considerable spectral efficiency improvement. Finally, in order to alleviate the negative impact of OAM mode offset on the system performance, a reduced dimensionality digital signal processing stage is integrated at the receiver through a ZF combiner.

APPENDIX A
PROOF FOR PROPOSITION 1

Given equations (1)–(4), and by leveraging the circulant channel matrix property and the time shift DFT property, the received signal at the m^{th} receive antenna (before combining) can be rewritten as

$$r_m = \sum_{n=0}^{N-1} h_{mn} x_n + n_m \tag{33}$$

$$= \sum_{n=0}^{N-1} h_{(n-m)_N} x_n + n_m \tag{34}$$

$$= \frac{1}{\sqrt{N}} \sum_{l=0}^{M-1} \sqrt{p_l} s_l \sum_{n=0}^{N-1} h_{(n-m)_N} e^{-j\frac{2\pi n l}{N}} + n_m \tag{35}$$

$$= \frac{1}{\sqrt{N}} \sum_{l=0}^{M-1} \sqrt{p_l} s_l e^{-j\frac{2\pi m l}{N}} \sum_{n=0}^{N-1} h_{(n-m)_N} e^{-j\frac{2\pi(n-m)l}{N}} + n_m \tag{36}$$

which upon recalling the fact that $\lambda_l = \sum_{n=0}^{N-1} h_{(n-m)_N} e^{-j\frac{2\pi(n-m)l}{N}}$, reduces to (13), and this concludes the proof.

APPENDIX B
PROOF FOR PROPOSITION 2

In the presence of a constant OAM mode offset of ϵ at the receive PSN, with the aid of the geometric summation formula $\sum_{m=0}^{N-1} a^m = \frac{1-a^N}{1-a}$, the received p^{th} OAM mode signal is then given by

$$y_p = \frac{1}{\sqrt{N}} \sum_{m=0}^{N-1} r_m e^{j\frac{2\pi(p+\epsilon)m}{N}} \tag{37}$$

$$= \frac{1}{N} \sum_{m=0}^{N-1} \sum_{l=0}^{M-1} \sqrt{p_l} \lambda_l s_l e^{-j\frac{2\pi m l}{N}} e^{j\frac{2\pi(p+\epsilon)m}{N}} + \widetilde{n}_p \tag{38}$$

$$= \frac{1}{N} \sum_{l=0}^{M-1} \sqrt{p_l} \lambda_l s_l \sum_{m=0}^{N-1} e^{j\frac{2\pi(p-l+\epsilon)m}{N}} + \widetilde{n}_p \tag{39}$$

$$= \frac{1}{N} \sum_{l=0}^{M-1} \sqrt{p_l} \lambda_l s_l \frac{1 - e^{j2\pi(p-l+\epsilon)}}{1 - e^{j\frac{2\pi}{N}(p-l+\epsilon)}} + \widetilde{n}_p \tag{40}$$

$$= \sum_{l=0}^{M-1} \lambda_l \sqrt{p_l} s_l \frac{1}{N} \frac{e^{j\pi(p-l+\epsilon)} \sin\left(\pi\left(p-l+\epsilon\right)\right)}{e^{j\frac{\pi}{N}(p-l+\epsilon)} \sin\left(\frac{\pi}{N}\left(p-l+\epsilon\right)\right)} + \widetilde{n}_p \tag{41}$$

$$= \sum_{l=0}^{M-1} \lambda_l \sqrt{p_l} s_l \frac{\operatorname{sinc}\left(p-l+\epsilon\right)}{\operatorname{sinc}\left(\frac{1}{N}\left(p-l+\epsilon\right)\right)} e^{j\frac{\pi}{N}(p-l+\epsilon)(N-1)} + \widetilde{n}_p \tag{42}$$

which upon letting $c(l,p) = \frac{\operatorname{sinc}(p-l+\epsilon)}{\operatorname{sinc}(\frac{1}{N}(p-l+\epsilon))} e^{j\frac{\pi}{N}(p-l+\epsilon)(N-1)}$, reduces to (14), and this concludes the proof.

REFERENCES

[1] A. Alkhateeb, J. Mo, N. Gonzalez-Prelcic, and R. W. Heath Jr., "MIMO precoding and combining solutions for millimeter-wave systems," *IEEE Commun. Mag.*, vol. 52, no. 12, pp. 122–131, Dec. 2014.

[2] A. Almradi, M. Matthaiou, P. Xiao, and V. F. Fusco, "Hybrid precoding for massive MIMO with low rank channels: A two-stage user scheduling approach," *IEEE Trans. Commun.*, vol. 68, no. 8, pp. 4816–4831, Aug. 2020.

[3] A. F. Molisch *et al.*, "Hybrid beamforming for massive MIMO: A survey," *IEEE Commun. Mag.*, vol. 55, no. 9, pp. 134–141, Sep. 2017.

[4] X. Gao, L. Dai, and A. M. Sayeed, "Low RF-complexity technologies to enable millimeter-wave MIMO with large antenna array for 5G wireless communications," *IEEE Commun. Mag.*, vol. 56, no. 4, pp. 211–217, Apr. 2018.

[5] W. Cheng, W. Zhang, H. Jing, S. Gao, and H. Zhang, "Orbital angular momentum for wireless communications," *IEEE Wireless Commun.*, vol. 26, no. 1, pp. 100–107, Feb. 2019.

[6] E. Basar, "Orbital angular momentum with index modulation," *IEEE Trans. Wireless Commun.*, vol. 17, no. 3, pp. 2029–2037, Mar. 2018.

[7] O. Edfors and A. J. Johansson, "Is orbital angular momentum (OAM) based radio communication an unexploited area?" *IEEE Trans. Antennas Propag.*, vol. 60, no. 2, pp. 1126–1131, Feb. 2012.

[8] R. Chen, H. Xu, M. Moretti, and J. Li, "Beam steering for the misalignment in UCA-based OAM communication systems," *IEEE Wireless Commun. Lett.*, vol. 7, no. 4, pp. 582–585, Aug. 2018.

[9] K. A. Opare, Y. Kuang, and J. J. Kponyo, "Mode combination in an ideal wireless OAM-MIMO multiplexing system," *IEEE Wireless Commun. Lett.*, vol. 4, no. 4, pp. 449–452, Aug. 2015.

[10] W. Zhang *et al.*, "Mode division multiplexing communication using microwave orbital angular momentum: An experimental study," *IEEE Trans. Wireless Commun.*, vol. 16, no. 2, pp. 1308–1318, Feb. 2017.

[11] Y. Ren *et al.*, "Line-of-sight millimeter-wave communications using orbital angular momentum multiplexing combined with conventional spatial multiplexing," *IEEE Trans. Wireless Commun.*, vol. 16, no. 5, pp. 3151–3161, May 2017.

[12] R. Chen, W. Yang, H. Xu, and J. Li, "A 2-D FFT-based transceiver architecture for OAM-OFDM systems with UCA antennas," *IEEE Trans. Veh. Technol.*, vol. 67, no. 6, pp. 5481–5485, Jun. 2018.

[13] L. Liang, W. Cheng, W. Zhang, and H. Zhang, "Joint OAM multiplexing and OFDM in sparse multipath environments," *IEEE Trans. Veh. Technol.*, vol. 69, no. 4, pp. 3864–3878, Apr. 2020.

[14] H. Jing, W. Cheng, W. Zhang, and H. Zhang, "Optimal UCA design for OAM based wireless backhaul transmission," in *Proc. IEEE Int. Conf. Commun.*, 2020, pp. 1–6.

[15] R. M. Gray, *Toeplitz and Circulant Matrices: A Review*. Boston, MA, USA: Now Publishers, 2006.

[16] R. Chen, W. X. Long, X. Wang, and L. Jiandong, "Multi-mode OAM radio waves: Generation, angle of arrival estimation and reception with UCAs," *IEEE Trans. Wireless Commun.*, vol. 19, no. 10, pp. 6932–6947, Oct. 2020.

[17] F. Shen, J. Mu, K. Guo, S. Wang, and Z. Guo, "Generation of continuously variable mode vortex electromagnetic waves with three dimensional helical antenna," *IEEE Antennas Wireless Propag. Lett.*, vol. 18, no. 6, pp. 1091–1095, Jun. 2019.

[18] G. Junkin, "A circularly polarized single-frequency multimode helical beam antenna," *IEEE Trans. Antennas Propag.*, vol. 67, no. 3, pp. 1459–1466, Mar. 2019.

[19] L. Kang, H. Li, J. Zhou, S. Zheng, and S. Gao, "A mode-reconfigurable orbital angular momentum antenna with simplified feeding scheme," *IEEE Trans. Antennas Propag.*, vol. 67, no. 7, pp. 4866–4871, Jul. 2019.

[20] M. A. B. Abbasi, V. F. Fusco, S. M. Abbas, and O. Malyuskin, "Alignment aspects of OAM signal reception using Rotman lens based circular array," in *Proc. IEEE 5G World Forum*, 2020, pp. 488–490.

[21] A. Almradi and K. A. Hamdi, "Spectral efficiency of OFDM systems with random residual CFO," *IEEE Trans. Commun.*, vol. 63, no. 7, pp. 2580–2590, Jul. 2015.

[22] A. Alkhateeb, O. El Ayach, G. Leus, and R. W. Heath Jr., "Channel estimation and hybrid precoding for millimeter wave cellular systems," *IEEE J. Sel. Topics Signal Process.*, vol. 8, no. 5, pp. 831–846, Oct. 2014.

[23] J. Lee, G. Gil, and Y. H. Lee, "Channel estimation via orthogonal matching pursuit for hybrid MIMO systems in millimeter wave communications," *IEEE Trans. Commun.*, vol. 64, no. 6, pp. 2370–2386, Jun. 2016.

[24] S. Park and R. W. Heath Jr., "Spatial channel covariance estimation for the hybrid MIMO architecture: A compressive sensing-based approach," *IEEE Trans. Wireless Commun.*, vol. 17, no. 12, pp. 8047–8062, Dec. 2018.

[25] D. Liu, L. Gui, Z. Zhang, H. Chen, G. Song, and T. Jiang, "Multiplexed OAM wave communication with two OAM mode antenna systems," *IEEE Access*, vol. 7, pp. 4160–4166, Dec. 2019.

[26] C. Xu *et al.*, "Free space radio communication employing OAM multiplexing based on Rotman lens," *IEEE Microw. Wireless Compon. Lett.*, vol. 26, no. 9, pp. 738–740, Sep. 2016.

[27] M. A. B. Abbasi, V. F. Fusco, U. Naeem, and O. Malyuskin, "Physical layer secure communication using orbital angular momentum transmitter and a single antenna receiver," *IEEE Trans. Antennas Propag.*, vol. 68, no. 7, pp. 5583–5591, Jul. 2020.

[28] R. C. Hansen, "Design trades for Rotman lenses," *IEEE Trans. Antennas Propag.*, vol. 39, no. 4, pp. 464–472, Apr. 1991.

[29] A. Chepala, Y. Ding, and V. F. Fusco, "Multimode circular antenna array for spatially encoded data transmission," *IEEE Trans. Antennas Propag.*, vol. 67, no. 6, pp. 3863–3868, Jun. 2019.

[30] A. Chepala, H. Tataria, and V. F. Fusco, "Beamspace modulated circular array," *IEEE Trans. Antennas Propag.*, vol. 67, no. 5, pp. 3496–3499, May 2019.

[31] B. Sheleg, "A matrix-fed circular array for continuous scanning," *Proc. IEEE*, vol. 56, no. 11, pp. 2016–2027, Nov. 1968.

[32] S. M. Mohammadi *et al.*, "Orbital angular momentum in radio-A system study," *IEEE Trans. Antennas Propag.*, vol. 58, no. 2, pp. 565–572, Feb. 2010.

[33] Y. Rahmat-Samii, V. Galindo-Israel, and R. Mittra, "A plane polar approach for far field construction from near field measurements," *IEEE Trans. Antennas Propag.*, vol. 28, no. 2, pp. 216–230, Mar. 1980.

[34] C. Guo, X. Zhao, C. Zhu, P. Xu, and Y. Zhang, "An OAM patch antenna design and its array for higher order OAM mode generation," *IEEE Antennas Wireless Propag. Lett.*, vol. 18, no. 5, pp. 816–820, May 2019.

[35] M. Herdin, N. Czink, H. Ozcelik, and E. Bonek, "Correlation matrix distance, a meaningful measure for evaluation of non-stationary MIMO channels," in *Proc. IEEE Veh. Technol. Conf.*, May 2005, pp. 136–140.

Ahmed Almradi received the B.Sc. degree in electrical and electronic engineering from the University of Tripoli, Tripoli, Libya, in 2004, the M.Sc. degree in electrical and electronic engineering from the Rochester Institute of Technology, Rochester, NY, USA, in 2012, and the Ph.D. degree in electrical and electronic engineering from The University of Manchester, Manchester, U.K, in 2017. From November 2017 to March 2019, he was a Postdoctoral Research Fellow with the 5G Innovation Centre, Institute for Communication Systems, University of Surrey, Guildford, U.K. From March 2019 to May 2021, he was a Postdoctoral Research Fellow with the Centre for Wireless Innovation, Queen's University Belfast, Belfast, U.K. He is currently with Wireless Research Team, BT Labs, Adastral Park, Ipswich, U.K. His current research interests include the modeling, design, and performance analysis of wireless communication systems, with special emphasis on multiuser massive MIMO in hybrid analog and digital precoding systems.

Muhammad Ali Babar Abbasi (Member, IEEE) received the B.S. degree in electrical engineering from COMSATS University, Islamabad, Pakistan, the M.S. degree in electrical engineering from the National University of Sciences and Technology, Islamabad, Pakistan, in 2013, and the Ph.D. degree in electrical engineering from Frederick University, Nicosia, Cyprus, in 2017. He is currently a Lecturer (Assistant Professor) with the Centre of Wireless Innovation (CWI), Queen's University Belfast, Belfast, U.K. From 2017 to 2019, he was a Research Fellow with CWI, working on mmWave radio hardware. He has authored or coauthored more than 60 journal and conference articles and contributed five book chapters. Dr. Abbasi was the recipient of the Erasmus Mundus INTACT Doctoral Scholarship by the European Union in 2014. He was the Grand Prize Winner in the Mobile World Scholar Challenge at the Mobile World Congress in 2019 (MWC19). He was a reviewer, session chair, and technical program committee member in a number of scientific conferences and workshops.

Michail Matthaiou (Senior Member, IEEE) was born in Thessaloniki, Greece, in 1981. He received the Diploma degree (5 years) in electrical and computer engineering from the Aristotle University of Thessaloniki, Greece, in 2004, the M.Sc. (with distinction) in communication systems and signal processing from the University of Bristol, U.K., in 2005, and the Ph.D. degree from the University of Edinburgh, Edinburgh, U.K., in 2008. From September 2008 to May 2010, he was with the Institute for Circuit Theory and Signal Processing, Munich University of Technology, Germany, working as a Postdoctoral Research Associate. He is currently a Professor of communications engineering and signal processing and the Deputy Director of the Centre for Wireless Innovation, Queen's University Belfast, U.K., after holding an Assistant Professor position with the Chalmers University of Technology, Sweden. His research interests include signal processing for wireless communications, beyond massive MIMO, intelligent reflecting surfaces, mm-wave/THz systems, and deep learning for communications. Dr. Matthaiou and his coauthors was the recipient of the IEEE Communications Society (ComSoc) Leonard G. Abraham Prize in 2017. He currently holds the ERC Consolidator Grant BEATRICE (2021–2026) focused on the interface between information and electromagnetic theories. He was awarded the prestigious 2018/2019 Royal Academy of Engineering/The Leverhulme Trust Senior Research Fellowship and was also the recipient of the 2019 EURASIP Early Career Award. His team was also the Grand Winner of the 2019 Mobile World Congress Challenge. He was the recipient of the 2011 IEEE ComSoc Best Young Researcher Award for the Europe, Middle East and Africa Region and the co-recipient of the 2006 IEEE Communications Chapter Project Prize for the best M.Sc. dissertation in the area of communications. He has coauthored papers that was the recipient of the Best Paper Awards at the 2018 IEEE WCSP and 2014 IEEE ICC and was an Exemplary Reviewer for IEEE COMMUNICATIONS LETTERS for 2010. In 2014, he received the Research Fund for International Young Scientists from the National Natural Science Foundation of China. He is currently the Editor-in-Chief of the *Elsevier Physical Communication*, a Senior Editor of the IEEE WIRELESS COMMUNICATIONS LETTERS and an Associate Editor for the IEEE JSAC SERIES ON MACHINE LEARNING FOR COMMUNICATIONS AND NETWORKS.

Vincent F. Fusco (Fellow, IEEE) received the bachelor's degree (Hons.) in electrical and electronic engineering, the Ph.D. degree in microwave electronics, and the D.Sc. degree from Queen's University Belfast (QUB), Belfast, U.K., in 1979, 1982, and 2000, respectively. He is currently the Director of research with ECIT Research Institute, QUB. He specialises in microwave through sub-millimetre front-end circuit architectures and self-tracking antennas. He has authored or coauthored more than 650 peer reviewed research papers, two books, and holds 12 patents. He is a Member of the Royal Irish Academy and a Fellow of the U.K. Royal Academy of Engineering, the Irish Academy of Engineering and also the Institution of Engineering Technology (IET) and is a Chartered Engineer. In 2012, he was awarded the IET Senior Achievement Award and the Mountbatten Medal, and the Royal Irish Academy Gold Medal for Engineering Sciences in 2019.